Water Research 88 (2016) 358–370

Contents lists available at ScienceDirect

Water Research

journal homepage: www.elsevier.com/locate/watres

Resistance identification and rational process design in Capacitive Deionization

J.E. Dykstra [a, b], R. Zhao [b, c], P.M. Biesheuvel [b, d, *], A. van der Wal [a]

[a] Department of Environmental Technology, Wageningen University, Bornse Weilanden 9, 6708 WG Wageningen, The Netherlands
[b] Wetsus, European Centre of Excellence for Sustainable Water Technology, Oostergoweg 9, 8911 MA Leeuwarden, The Netherlands
[c] Engineering Research Center for Nanophotonics & Advanced Instrument, Ministry of Education, Department of Physics, East China Normal University, 3663 North Zhongshan Road, 200062 Shanghai, China
[d] Laboratory of Physical Chemistry and Soft Matter, Wageningen University, Dreijenplein 6, 6703 HB Wageningen, The Netherlands

ARTICLE INFO

Article history:
Received 8 June 2015
Received in revised form
24 September 2015
Accepted 2 October 2015
Available online 9 October 2015

Keywords:
Capacitive Deionization
Water desalination
Porous carbon electrodes
Ion-exchange membranes
Electronic resistances

ABSTRACT

Capacitive Deionization (CDI) is an electrochemical method for water desalination employing porous carbon electrodes. To enhance the performance of CDI, identification of electronic and ionic resistances in the CDI cell is important. In this work, we outline a method to identify these resistances. We illustrate our method by calculating the resistances in a CDI cell with membranes (MCDI) and by using this knowledge to improve the cell design. To identify the resistances, we derive a full-scale MCDI model. This model is validated against experimental data and used to calculate the ionic resistances across the MCDI cell. We present a novel way to measure the electronic resistances in a CDI cell, as well as the spacer channel thickness and porosity after assembly of the MCDI cell. We identify that for inflow salt concentrations of 20 mM the resistance is mainly located in the spacer channel and the external electrical circuit, not in the electrodes. Based on these findings, we show that the carbon electrode thickness can be increased without significantly increasing the energy consumption per mol salt removed, which has the advantage that the desalination time can be lengthened significantly.

1. Introduction

Capacitive Deionization (CDI) is an electrochemical desalination technology which employs porous carbon electrodes to adsorb ions from water (Jung et al., 2007; Tsouris et al., 2011; Huang et al., 2012; Rica et al., 2012; Kim and Yoon, 2013; Mossad and Zou, 2013; Zhao et al., 2013a; Omosebi et al., 2014; Lei et al., 2015; Tang et al., 2015). Upon applying a voltage difference between two electrodes, cations are adsorbed from the water into the negatively polarized electrode (cathode), while anions are adsorbed into the positively polarized electrode (anode). During this adsorption step, or charging step, feed water flows through the cell and is desalinated, resulting in a deionized water effluent. After the electrodes are saturated, the electrodes are short-circuited and ions are released, which is called the desorption or discharging step.

During the adsorption step, ions are stored in electrical double layers (EDLs) formed in the carbon electrodes (Giera et al., 2015; Prehal et al., 2015). For every electron transported from one electrode to the other, a counterion can adsorb in these EDLs in both electrodes, or a co-ion can desorb (Biesheuvel et al., 2014; Kim et al., 2015). Whereas the adsorption of counterions is desired and leads to salt adsorption, the desorption of the co-ions is undesired. In order to increase the salt adsorption, a cation exchange membrane (CEM) is placed in front of the cathode, and an anion exchange membrane (AEM) in front of the anode (Zhao et al., 2012; Choi, 2014; van Limpt and van der Wal, 2014; Kim and Choi, 2010; Lee et al., 2006). These ion exchange membranes allow the passage of counterions and hinder co-ions, which enhances the desalination performance. The CDI technology including membranes in the cell configuration, is referred to as Membrane Capacitive Deionization (MCDI).

CDI cells with various electrode configurations have been proposed, such as flow-through electrodes (Avraham et al., 2009; Suss et al., 2012), flowable carbon slurries (Jeon et al., 2013; Suss et al., 2015), or wire-shaped electrodes (Porada et al., 2012). In the present work we focus on a cell configuration using static film electrodes, where the water flows between the two planar electrodes. In this configuration, the ion exchange membranes are placed

* Corresponding author. Wetsus, European Centre of Excellence for Sustainable Water Technology, Oostergoweg 9, 8911 MA Leeuwarden, The Netherlands.
E-mail address: maarten.biesheuvel@wetsus.nl (P.M. Biesheuvel).

http://dx.doi.org/10.1016/j.watres.2015.10.006
0043-1354/

between the spacer channel and the electrodes, as shown in Fig. 1. On the other side of the electrode, we place current collectors which are connecting the electrodes with the external electrical circuit.

To improve the performance of the CDI technology, it is important to identify where are the resistances in the cell (Li et al., 2010; Długołęcki and van der Wal, 2013; Demirer et al., 2013; Qu et al., 2015; Zhao et al., 2014). This knowledge can be used to reduce energy consumption and optimize the cell design. To this end, we have to quantify the contribution of the different elements of the cell to the total resistance, from which the energy losses can be calculated. In the present work, we will separate the resistances in two types: I) the electronic resistances, which are related to the transport of electrons and thus located in the cables, current collectors and carbon matrix in the electrodes, and II) the ionic resistances, which are related to the ion transport and thus located in the pores of the electrodes, in the membranes and in the spacer channel. These electronic and ionic resistances result in voltage drops over the different elements of the cell, see Fig. 1.

In the present work, we will address the following issues: I) to present a methodology to identify and quantify the electronic and ionic resistances in the different elements in a CDI cell, and II) to show how such knowledge can be used to rationally design improvements in CDI architecture and operation. As an example, we illustrate our method by calculating resistances in a laboratory scale MCDI cell, i.e. a CDI cell including membranes.

The ionic resistances are mainly dependent on the local salt concentration, i.e., higher salt concentrations result in lower resistances. Therefore, we have to calculate the salt concentration profiles across the spacer channel, the membranes and the electrodes during operation of the MCDI cell, in order to quantify the ionic resistances over these elements. The transmission line (TL) theory proposed by de Levie (1963) was used by Posey and Morozumi (1966) to describe charge transport in a porous electrode, and extended by Johnson and Newman (1971) to the case of desalination. However, the TL theory is derived for electrodes at constant and high salt concentrations. Since CDI is typically operated at lower salt concentrations, the TL theory is not suitable for CDI and must be extended (Biesheuvel et al., 2014; Mirzadeh et al., 2014). In this extension of the TL theory, we combine an accurate model for the structure of the EDL in the micropores of the carbon electrode (Biesheuvel et al., 2014) with a model for the transport of ions across the entire porous carbon electrode. This electrode model is combined with a transport model for ions across the spacer channel and membranes, as function of time.

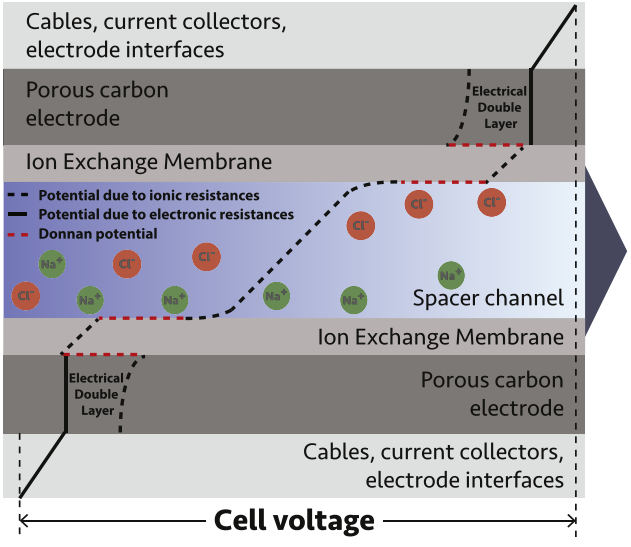

Fig. 1. Qualitative overview of the potential profiles across a membrane Capacitive Deionization cell, showing the different elements.

In order to use this model to calculate the ionic resistances in the cell, several input parameters should be determined. In the present work, we present an experimental procedure, including a novel approach to determine the thickness and the porosity of the compressed spacer channel inside the MCDI cell. The next step is to verify the model by comparing simulation results with constant current charging/discharging experiments. The validated model is subsequently used to predict the resistances across the MCDI cell. Based on the information obtained from these simulations we recommend an improved cell design, which is experimentally verified. In particular, for the tested cell geometry, one recommendation is that one can double or triple the thickness of the electrodes, and thus have longer periods of desalination, while the energy costs per mol salt removed are not significantly increased.

2. Theory

In the present work, we combine two models, the improved modified Donnan (i-mD) model, and a transport model. The i-mD model describes the EDLs formed in the carbon micropores and relates the charge density, salt adsorption and potential to one another. The transport model calculates the transport of ions from the spacer channel, through the membranes, into the porous carbon electrodes; thus the transport is described in the direction perpendicular to the flow channel. In the electrode, we model two different phenomena: I) the transport of salt across the electrode through the macropores and, II) the simultaneous adsorption of ions into the micropores, where the EDLs are formed. The i-mD model (Biesheuvel et al., 2014; Kim et al., 2015) is discussed in Appendix A. The transport model is described next.

To derive the transport model, we will make three simplifications. Firstly, we model a symmetric MCDI cell, which means that the anode has the same characteristics, regarding geometrical dimensions and porosity, as the cathode, except for the sign of the charge. The same holds for the membranes, i.e. the AEM has the same properties, regarding its dimensions, porosity and membrane charge, as the CEM, except for the sign of the membrane charge. Secondly, we only model the adsorption and transport of KCl, for which we assume the cation and the anion to have the same diffusion coefficient in all elements of the cell. Finally, we assume that only capacitive processes occur in the electrodes, and no electrochemical reactions take place (Bouhadana et al., 2011; Lee et al., 2010). These simplifications allow us to model only half of the cell, so we only consider half of a spacer channel, that is from the spacer midplane to the spacer-membrane boundary, one membrane and one electrode.

2.1. Porous carbon electrodes

In the electrodes, we distinguish three different types of pores. Firstly, we consider the micropores, where EDLs are formed and ions are stored. Secondly, we describe the macropores, which are used as transport pathways for the ions to go from the membrane-electrode boundary to the micropores. Thirdly, to account for immobile pore space within the carbon particles where neither ions are stored in EDLs nor ions are transported, we include mesopores in the model, which contain charge-neutral electrolyte, at the same concentration as in the macropores (Kim et al., 2015).

The molar flux of ions through the macropores, subject to diffusional and migrational forces, is given by the Nernst–Planck equation

$$J_i = -D_i \cdot \left(\frac{\partial c_{mA,i}}{\partial x} + z_i \cdot c_{mA,i} \cdot \frac{\partial \phi_{mA}}{\partial x} \right), \tag{1}$$

where subscript i refers to ion type i, and where J_i is the molar ion flux in mol/m^2/s, D_i the ion diffusion coefficient in m^2/s, $c_{mA,i}$ the ion concentration in the macropores in mol/m^3, ϕ_{mA} the dimensionless potential in the macropores, and x the coordinate running from the membrane-electrode boundary to the electrode-current collector boundary.

Across the electrode, we evaluate the ion mass balance

$$\frac{\partial}{\partial t} \left((p_{mA} + p_{meso}) \cdot c_{mA,i} + p_{mi} \cdot c_{mi,i} \right) = -p_{mA} \cdot \frac{\partial J_i}{\partial x}, \tag{2}$$

where p_{mA}, p_{meso}, and p_{mi} are the macro-, meso- and microporosity of the electrode, and $c_{mi,i}$ is the ion concentration in the micropores.

Furthermore, we need the electroneutrality condition for the macro- and mesopores

$$\sum_i z_i \cdot c_{mA,i} = 0, \tag{3}$$

where Σ_i describes a summation over all ions in the system, i.e. K^+ and Cl^-, just as in Eqs. (4), (17) and (18).

The micropore charge density, σ_{mi}, and micropore ions concentration, $c_{ions,mi}$ are defined as

$$\begin{aligned} \sigma_{mi} &= \sum_i z_i \cdot c_{mi,i}, \\ c_{ions,mi} &= \sum_i c_{mi,i}. \end{aligned} \tag{4}$$

Based on Eqs. (1)–(4), we derive two balance equations describing the evolution of σ_{mi} and c_{mA} as function of time. First, we set up the micropore charge balance evaluating σ_{mi} over time by combining Eqs. (1)–(4), which results in

$$p_{mi} \cdot \frac{\partial \sigma_{mi}}{\partial t} = 2 \cdot p_{mA} \cdot D \cdot \frac{\partial}{\partial x} \left(c_{mA} \cdot \frac{\partial \phi_{mA}}{\partial x} \right), \tag{5}$$

where c_{mA} is the salt concentration in the macro- and mesopores, which is equal to the ion concentration of K^+ and that of Cl^-. Parameter D is the diffusion coefficient of K^+ and Cl^-, which are assumed to be equal to one another.

Second, Eqs. (1) and (3) are substituted in Eq. (2), and summed over the cat- and the anion, resulting in the salt mass balance

$$\frac{\partial}{\partial t} \left(2 \cdot (p_{mA} + p_{meso}) \cdot c_{mA} + p_{mi} \cdot c_{ions,mi} \right) = 2 \cdot p_{mA} \cdot D \cdot \frac{\partial^2 c_{mA}}{\partial x^2}. \tag{6}$$

Across the electrode, at each position, ϕ_{mA} is related to the potential in the carbon matrix, ϕ_1, the Donnan potential, $\Delta\phi_D$, and the Stern potential, $\Delta\phi_{St}$. These potentials follow from the i-mD model (see Appendix A). The potentials ϕ_{mA} and ϕ_1 are related to $\Delta\phi_D$ and $\Delta\phi_{St}$ by

$$\phi_1 - \phi_{mA} = \Delta\phi_D + \Delta\phi_{St}. \tag{7}$$

In this work, we assume that there is no electronic resistance across the electrode, see Appendix B. Consequently, the measured electronic resistance can only be located in the external circuit. The external circuit includes the cables, current collectors, and the interface between the current collectors and electrodes. From now on, we call the sum of these resistances the external electronic resistance, EER, with dimension Ω m^2. The assumption that there is no electronic resistance in the electrodes leads to a position invariant value of ϕ_1, and allows us to relate ϕ_1 to the cell voltage (see Fig. 1), V_{cell}, by

$$V_{cell} = 2 \cdot \phi_1 \cdot V_T + I \cdot EER, \tag{8}$$

where I is the current density (A/m^2). The thermal voltage, V_T, is given by $V_T = R \cdot T/F$, where R is the gas constant (8.314 J/(mol·K)), T the temperature (K) and F Faraday's constant (96,485 C/mol). Note that Eq. (8) requires the assumption of symmetry, which allows us to model only half of the cell with the potential at the spacer midplane set to zero.

We define an ionic resistance across the two electrodes in an MCDI cell, R_{mA}, with dimension Ω m^2, according to

$$R_{mA} \cdot I = 2 \cdot \Delta\phi_{mA} \cdot V_T, \tag{9}$$

where $\Delta\phi_{mA}$ is $\phi_{mA}|_{E/C}$, the macropore potential at the electrode – current collector boundary (E/C), minus $\phi_{mA}|_{M/E}$, the potential at the membrane-electrode boundary (M/E).

At the E/C interface, we apply the boundary conditions

$$\left. \frac{\partial c_{mA}}{\partial x} \right|_{E/C} = 0, \quad \left. \frac{\partial \phi_{mA}}{\partial x} \right|_{E/C} = 0, \tag{10}$$

while those at the M/E interface will be described in Section 2.3.

2.2. Spacer channel

Our model for the spacer channel is as follows. In the flow direction, we describe the development of concentration profiles between the out- and inflow of the cell. To that end, we divide the spacer channel in M sequential mathematical subcells, see Fig. 2 in the work of Zhao et al. (2013b). In this approach, the electrolyte flows downstream from subcell i into subcell $i+1$; therefore, the inflow salt concentration in subcell $i+1$ equals the effluent concentration of subcell i. The effluent salt concentration of the MCDI cell is equal to the concentration in subcell M. For every subcell, we calculate the transport of salt and charge into the electrodes, and the salt concentration in the spacer channel, using Eqs. (5) and (6).

Also, in the spacer channel concentration profiles develop between the spacer midplane and the membrane, thus in the direction perpendicular to the flow direction. To model these concentration profiles, we set up the following salt mass balance to be solved in each subcell of the spacer channel

$$p_{sp} \cdot \frac{\partial c_{sp}}{\partial t} = p_{sp} \cdot D \cdot \frac{\partial^2 c_{sp}}{\partial x^2} + \Gamma_{sp}, \tag{11}$$

where c_{sp} and p_{sp} are the salt concentration and porosity of the spacer channel. The coordinate x runs from the spacer midplane to the edge with the membrane. Dependent on the experiment, Γ_{sp} has a different form:

- In case we model experiments without a flow through the spacer channel (Section 4), Γ_{sp} describes a diffusive transport of salt into the spacer channels from outside (from the outer volume within the housing containing the MCDI cells), V_{out}. In this case Γ_{sp} is given by

$$\Gamma_{sp} = \gamma_{sp} (c_{out} - c_{sp}), \tag{12}$$

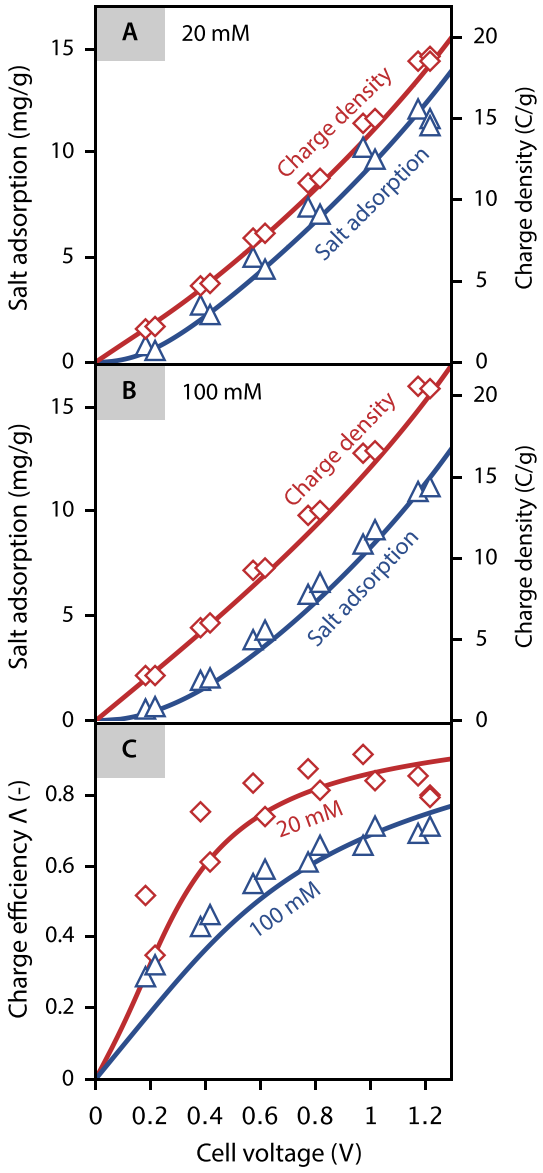

Fig. 2. Equilibrium data and theory of the salt adsorption and charge density as function of the cell voltage for a KCl solution. a) 20 mM. b) 100 mM. c) Charge efficiency Λ. Salt adsorption in mg/g based on molar mass of KCl.

where γ_{sp} describes the rate of ion diffusion, and c_{out} is the concentration in V_{out}, which is a constant equal to the initial value of c_{sp}.

- In case we model experiments with flow through the spacer channel (sections 5 and 6), Γ_{sp} is given by

$$\Gamma_{sp} = \frac{\Phi_v \cdot M}{A_{cell} \cdot L_{sp}} \left(c_{inflow} - c_{sp} \right), \tag{13}$$

where Φ_v is the water flowrate through the cell and A_{cell} the surface area of one electrode. For subcell $i = 1$, the salt concentration c_{inflow} is equal to the inflow concentration of the MCDI cell, while for $i > 1$, c_{inflow} is equal to the value for c_{sp} of subcell $i - 1$. Note that we assume an equal flowrate (water velocity), across the spacer channel, i.e., independent of x.

At the spacer midplane (S^*), we apply the boundary condition

$$\left. \frac{\partial c_{sp}}{\partial x} \right|_{S^*} = 0, \tag{14}$$

where we set ϕ_{sp}. For the spacer–membrane interface, boundary conditions are described in section 2.3.

The current density, I, is related to the ionic resistance over the spacer channel, R_{sp}, with dimension $\Omega\ \mathrm{m}^2$, by

$$R_{sp} \cdot I = 2 \cdot \Delta\phi_{sp} \cdot V_T, \tag{15}$$

where $\Delta\phi_{sp}$ is the potential difference over half the spacer channel. R_{sp} is given by

$$R_{sp} = \frac{L_{sp} \cdot V_T}{2 \cdot p_{sp} \cdot D \cdot F \cdot \langle c_{sp} \rangle} \tag{16}$$

where $\langle c_{sp} \rangle$ is the average salt concentration in the spacer channel.

2.3. Membranes

Across the membranes, we evaluate the total ion concentration, $c_{T,m}$, which is the summation of the concentration of the counter-ions and co-ions (Dykstra et al., 2014; Galama et al., 2013; Paz-Garcia et al., 2015). For the membranes, we can set up the salt mass balance

$$p_m \cdot \frac{\partial c_{T,m}}{\partial t} = -p_m \cdot \sum_i \left(\frac{\partial J_{i,m}}{\partial x} \right), \tag{17}$$

where p_m is the porosity of the membrane, and x the location in the membrane, running from the spacer-membrane boundary, S/M, to the membrane-electrode boundary, M/E. The flux $J_{i,m}$ is given by Eq. (1) (with subscript "mA" replaced by "m"). The diffusion coefficient D in Eq. (1) is replaced by $d_{r,m} \cdot D$. This factor $d_{r,m}$ reduces the diffusion coefficient in the membrane relative to the value in free solution, D. In the membranes, electroneutrality is assumed, given by

$$\sum_i (z_i \cdot c_{m,i}) + \omega X = 0, \tag{18}$$

where ωX is the membrane charge density in $\mathrm{mol/m^3}$, defined per unit aqueous solution in the membrane. Substituting Eq. (1) into Eq. (17), and assuming electroneutrality, results in

$$p_m \cdot \frac{\partial c_{T,m}}{\partial t} = p_m \cdot d_{r,m} \cdot D \cdot \left(\frac{\partial^2 c_{T,m}}{\partial x^2} - \omega X \cdot \frac{\partial^2 \phi_m}{\partial x^2} \right). \tag{19}$$

At the S/M and M/E boundaries, we have continuity of the salt flux,

$$\begin{aligned} -2 \cdot p_{sp} \cdot \left. \frac{\partial c_{sp}}{\partial x} \right|_{S/M} &= -d_{r,m} \cdot p_m \cdot \left(\frac{\partial c_{T,m}}{\partial x} - \omega X \frac{\partial \phi_m}{\partial x} \right) \Big|_{S/M}, \\ -2 \cdot p_{mA} \cdot \left. \frac{\partial c_{mA}}{\partial x} \right|_{M/E} &= -d_{r,m} \cdot p_m \cdot \left(\frac{\partial c_{T,m}}{\partial x} - \omega X \cdot \frac{\partial \phi_m}{\partial x} \right) \Big|_{M/E}. \end{aligned} \tag{20}$$

The current density, I, equals F times the molar flux of ionic charge, which is the sum of the molar ion fluxes times the ion valency. For instance, evaluating I in the membrane, at the M/E boundary, we obtain

$$I = -d_{r,m} \cdot D \cdot F \cdot c_{T,m} \cdot \left. \frac{\partial \phi_m}{\partial x} \right|_{M/E}. \tag{21}$$

On the outer surface of the two membranes, the following two conditions apply. I) The concentration $c_{T,m}$ relates to the salt concentration just outside the membrane, according to

$$c_{T,m}^2\Big|_{S/M} = X^2 + 4\cdot c_{sp}^2\Big|_{S/M},$$
$$c_{T,m}^2\Big|_{M/E} = X^2 + 4\cdot c_{mA}^2\Big|_{M/E}. \quad (22)$$

In addition, II) a Donnan potential develops at the membrane interfaces, given by

$$\omega X = 2\cdot c_{sp}|_{S/M}\cdot\sinh\left(\Delta\phi_{D,S/M}\right),$$
$$\omega X = 2\cdot c_{mA}|_{M/E}\cdot\sinh\left(\Delta\phi_{D,M/E}\right). \quad (23)$$

The ionic resistance summed over the two membranes in an MCDI cell, together R_m, with dimension $\Omega\ m^2$, is given by

$$R_m\cdot I = 2\cdot\Delta\phi_m\cdot V_T, \quad (24)$$

where $\Delta\phi_m$ is defined as $\Delta\phi_m = \phi_m|_{M/E} - \phi_m|_{S/M}$.

Lastly, we relate the potential in the macropores at the M/E boundary, $\phi_{mA}|_{M/E}$, to the potential over the spacer channel, the Donnan potentials on both sides of the membrane, and the potential drop over the membranes according to

$$\Delta\phi_{sp} + \Delta\phi_{D,S/M} + \Delta\phi_m - \Delta\phi_{D,M/E} = \phi_{mA}\Big|_{M/E}. \quad (25)$$

3. Characterization: electrode salt adsorption, electronic resistances and spacer properties

3.1. Electrode salt adsorption

Our methodology to identify the resistances in the MCDI cell makes uses of the transport model including the i-mD model, to calculate the values for the ionic resistances in the different elements of the MCDI cell. To run this model, we have to determine values of the parameters required in the i-mD model, which are E, ν_{mi}, $C_{St,vol,0}$ and α. Therefore, we conduct constant voltage experiments as described in Appendix D and by Kim et al. (2015), and we fit the i-mD model to the equilibrium data for salt adsorption, charge density and charge efficiency, which is the ratio of salt adsorption over charge density, see Fig. 2.

Fig. 2 shows that we find a good fit of the theory to the data using values for ν_{mi}, E, $C_{St,vol,0}$ and α as listed in Table 1. For the transport model, we also need values for the micro-, meso- and macroporosity, as listed in Table 1. Kim et al. (2015) and Appendix E describe how these porosities are calculated.

3.2. Electronic resistances and spacer properties

Before we run the transport model to calculate the ionic resistances across the MCDI cell, we will first determine the external electronic resistance, *EER*, which is located in the cables, current collectors and current collector–electrode interfaces (as discussed in section 2, we assume that there is no electronic resistance in the electrodes, see results in Appendix B which underpin this assumption.) Furthermore, as the thickness, L_{sp}, and porosity, p_{sp}, of the spacer channel are of influence to the ionic resistance in the spacer channel, R_{sp}, according to Eqs. (15) and (16), these parameters should be accurately determined as well. Since the (M)CDI stack (assembly of N_s cells), including the spacer channels, is slightly compressed by exerting a pressure of 0.29 bar, the thickness and porosity of the spacer channels after assembly are different from the values in uncompressed condition. In this section, we present a method to determine simultaneously *EER* as well as R_{sp}. In addition, we show how p_{sp} and L_{sp} after assembly can be calculated from R_{sp}.

We measure the resistance over a CDI stack, consisting of N_s cells and thus N_s spacer channels, using a Milliohmmeter, see Appendix B. This device does not measure an ionic distributed resistance in the electrodes as the electronic electrode resistance is very low, see Appendix B. Thus, the measured resistance over the CDI stack is a sum of the linear resistances *EER* and R_{sp}. How can we distinguish between *EER* and R_{sp}, and then, based on R_{sp}, calculate L_{sp} and p_{sp}? First we multiply the measured resistance by N_s and A_{cell} to obtain R^*, which is the sum of R_{sp} and *EER*. Because only R_{sp} depends on the electrolyte concentration, c_∞, we can distinguish between R_{sp} and *EER* from the dependence of R^* on c_∞, see Fig. 3. Resistance *EER* is not dependent on c_∞, and follows as the intercept of the curve in Fig. 3 ($EER = 7.0\ \Omega\ cm^2$).

The thickness and porosity L_{sp} and p_{sp} after assembly can be obtained from Fig. 3 as follows. First of all, R_{sp} is a function of L_{sp} and p_{sp} (after assembly) according to

$$R_{sp} = \frac{V_T\cdot L_{sp}}{2\cdot F\cdot p_{sp}\cdot c_\infty\cdot D}. \quad (26)$$

Secondly, p_{sp} and L_{sp} are related to the uncompressed thickness and porosity of the spacer channel, $L_{sp,uncompr}$ and $p_{sp,uncompr}$, as listed in Table 1, according to

$$\left(1 - p_{sp}\right)\cdot L_{sp} = \left(1 - p_{sp,uncompr}\right)\cdot L_{sp,uncompr}. \quad (27)$$

Finally, the slope of the curve in Fig. 3, β, relates to R_{sp}, by

$$\beta = R_{sp}\cdot c_\infty. \quad (28)$$

Substituting Eq. (27) into Eq. (26) and solving the resulting equation with Eq. (28), results in $L_{sp} = 316\ \mu m$ and $p_{sp} = 0.708$, see Table 1.

4. Verification: charging and discharging dynamics

In the previous section, we determined the values of parameters required to describe the salt adsorption in the EDLs of the porous carbon electrodes, as well as the external electronic resistance of the CDI cell and the compressed thickness and porosity of the spacer channel, as listed in Table 1. These parameters serve as input for the transport model, which calculates the concentration profiles across the spacer channel, the membranes, and the electrodes, and moreover, the ionic resistances in these different elements. However, before we run the model, we have to verify whether the transport model fits with experimental data.

To that end, we conduct constant current charging/discharging (CCCD) experiments for CDI and MCDI, with and without flowing an electrolyte through the cell (F-CCCD and NF-CCCD respectively), see Fig. 4. The experimental scheme is as follows. Before we start the experiment, we flush a salt solution with a concentration of 500, 100 or 20 mM KCl through the cell and we short-circuit the cell. For the NF-CCCD experiments (Fig. 5A–E), we stop the pump after about 10 min, while for the F-CCCD experiments we leave the pump running with a flowrate of 7.5 mL/min per cell. Thereafter, we apply a constant current to charge the cell until a cell voltage of 1.4 V is reached, and then, we apply the reversed current to discharge the cell until we reach a cell voltage of 0 V (Pell et al., 2000). This cycle, of charging and discharging the cell, is repeated 4 times to reach the limit cycle, which means that the cell voltage signal as function of time of the last cycle is equal to that of the previous cycle. Experiments were run at system currents of 0.25, 0.5, 0.75 and 1 A during the charging step and the reversed current during the discharging step. With the cell area of $A_{cell} = 33.8\ cm^2$ and $N_s = 4$ cells, this recalculates to current densities of $I = 19$, 37, 56 and 74 A/m^2.

The experimental limit cycles in an (M)CDI cell for different

Table 1
System and electrode dimensions, operational parameters, parameters used for theoretical calculations. Parameters obtained from *1) equilibrium model fitting, as discussed in Section 3.1; *2) external electronic resistances and spacer properties characterization, as discussed in section 3.1; *3) Ref. Porada et al. (2013); *4) Ref. Galama et al. (2013); *5) transport model calculations, as discussed in Section 4.

Experimental parameters			
L_{elec}	Electrode thickness	257 μm	
L_m	Membrane thickness	160 μm	
A_{cell}	Electrode geometric surface area	33.8 cm^2	
Φ_v	Flowrate through the cell	7.5 mL/min	
N_s	Number of cells in the MCDI stack	4	
T	Temperature	295 K	
ρ_{elec}	Electrode mass density	0.569 g/mL	
Values for use in the i-mD model			
E	Micropore ion-correlation energy	100 kT mol m^{-3}	*1
v_{mi}	Micropore volume	0.40 mL/g	*1
$C_{St,vol,0}$	Stern capacitance in zero-charge limit	160 F/mL	*1
α	Charge dependence of Stern capacitance	20 F m^3 mol^{-2}	*1
Electronic resistance and spacer channel properties			
EER	External electronic resistance (4 cells)	7.0 Ω cm^2	*2
L_{sp}	Thickness spacer, after assembly	316 μm	*2
p_{sp}	Porosity spacer, after assembly	0.708	*2
$L_{sp,uncompr}$	Thickness spacer, before assembly	335 μm	
$p_{sp,uncompr}$	Porosity spacer, before assembly	0.724	
Values for use in the transport model			
D	Diffusion coefficient of K^+, and of Cl^- in free solution	2.03 *10^{-9} m^2/s	
p_{mA}	Macroporosity	0.43	*1
p_{meso}	Mesoporosity	0.05	*1
p_{mi}	Microporosity	0.23	*1
p_{sk}	Fraction skeleton material electrode	0.29	*3
p_m	Membrane porosity	0.3	*4
$d_{r,m}$	Diffusion coefficient in the membrane relative to the value in free solution	0.05	*4
ω	Sign of the fixed membrane charge	+1	*4
X	Fixed membrane charge density	5 M	*4
γ_{sp}	Transport coefficient of salt from the outer volume into the spacer channel	0.26 mmol/s	*5
M	Number of mathematical subcells	1	

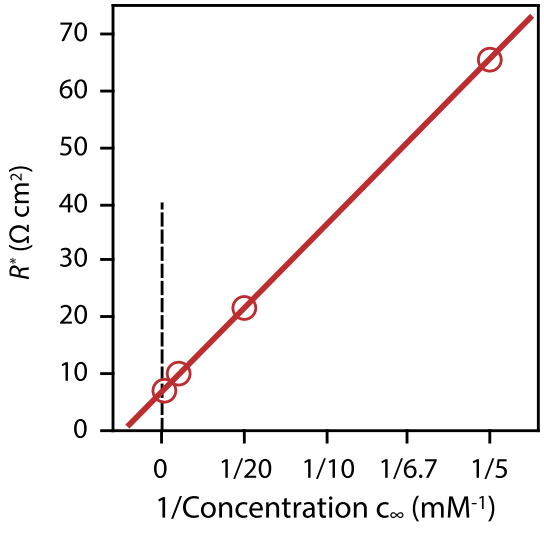

Fig. 3. Measured resistance in a CDI cell as function of the electrolyte concentration.

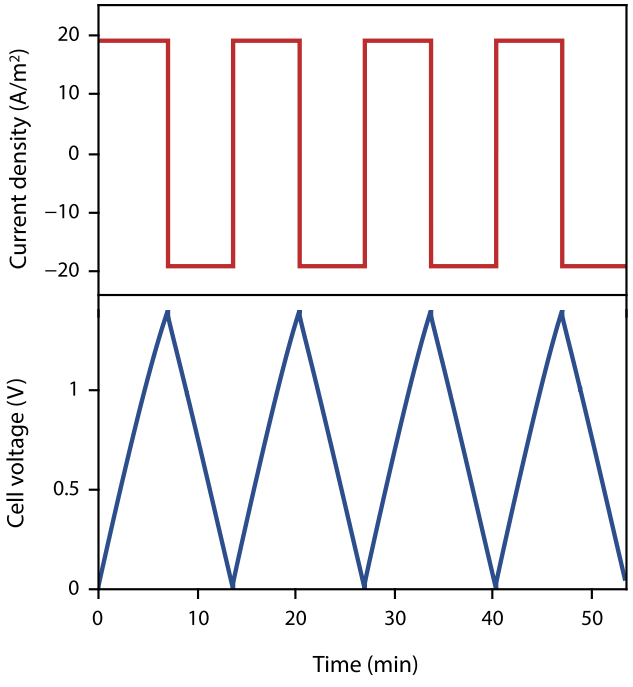

Fig. 4. Current density and cell voltage signal of constant current charging and discharging cycles in a CDI cell without flow (NF-CCCD), and with $c_{\infty,ini}$ = 500 mM. The current was 19 A/m^2 during the charging step and −19 A/m^2 during the discharging step.

electrolyte concentrations are compared with the theoretical limit cycles, as calculated with the transport model, in Fig. 5. The x-axes of the graphs in Fig. 5 include breaks, dividing the x-axes in two parts with different timescales. For the NF-CCCD experiments, in order to fit the theoretical curves to the data, we had to include a diffusion term, Γ_{sp}, in the spacer channel mass balance, Eq. (11), to describe some diffusion of salt from V_{out} into the spacer channel. We found the best fit of the theory with γ_{sp}, the transport coefficient, at a value of $\gamma = 0.26$ mmol/s. Fig. 5 shows that for these NF-CCCD experiments, the transport model fits the experimental data well, both for CDI and MCDI, especially at the higher initial salt concentrations ($c_{\infty,ini}$) of 100 and 500 mM KCl. However, as observed in Fig. 5E, for CDI with the initial salt concentration of 20 mM the fit is not as good: though the cycle time is well predicted, the cell voltage in the plateau region of the charging step is underestimated.

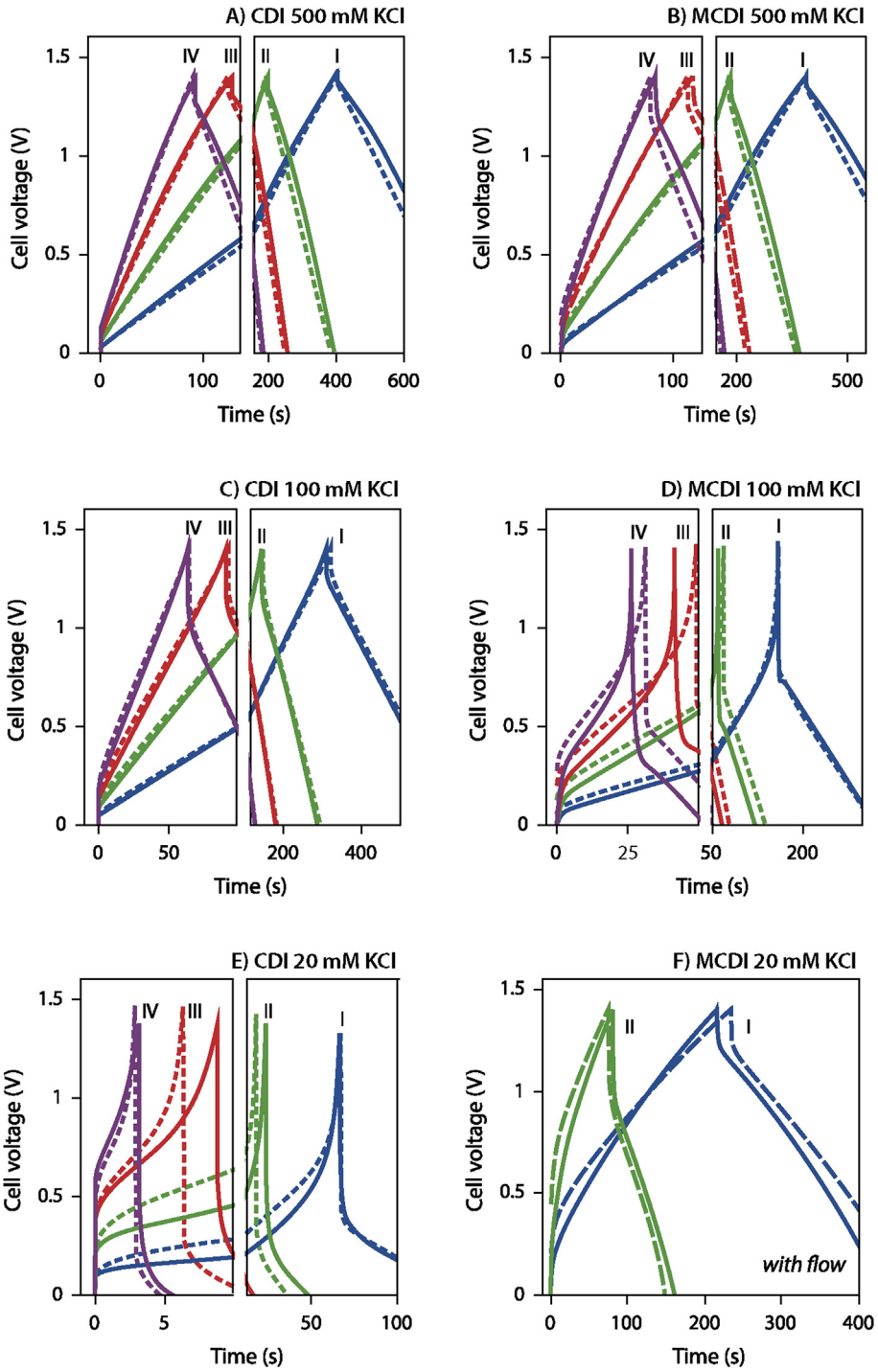

Fig. 5. Charge/discharge cycles for CDI and MCDI with initial salt concentrations of 500, 100 and 20 mM KCl (A-E, NF-CCCD), and with an inflow salt concentration of $c_{inflow} = 20$ mM (F, F-CCCD). Dashed lines: experimental data. Solid lines: theory. I) 19 A/m^2, II) 37 A/m^2, III) 56 A/m^2 and IV) 74 A/m^2.

As NF-CCCD MCDI experiments with an initial salt concentration of 20 mM KCl could not be fitted successfully, we report data and theory of F-CCCD experiments,[1] for which $c_{inflow} = 20$ mM KCl. The discrepancy between data and theory for MCDI NF-CCCD at 20 mM can be ascribed to the fact that the overlimiting current was reached, a phenomenon not included in our theory (Andersen et al., 2012). As shown in Fig. 5F, the model describes the data accurately for 20 mM F-CCCD experiments.

5. Prediction: resistances across the MCDI cell

After presenting the methodology to obtain values for the parameters required in the transport model (Section 3), and verifying

[1] Compared to the NF-CCCD experiments as shown in Fig. 5, for the F-CCCD experiments, the electrodes were thicker ($L_{elec} = 266$ μm instead of $L_{elec} = 257$ μm) and the mass density was lower ($\rho_{elec} = 0.395$ g/mL instead of $\rho_{elec} = 0.569$ g/mL). Therefore, p_{mA}, p_{meso} and p_{mi} have different values from the ones listed in Table 1, respectively 0.61, 0.031 and 0.16. These values are also used in the calculations in Figs. 7 and 8.

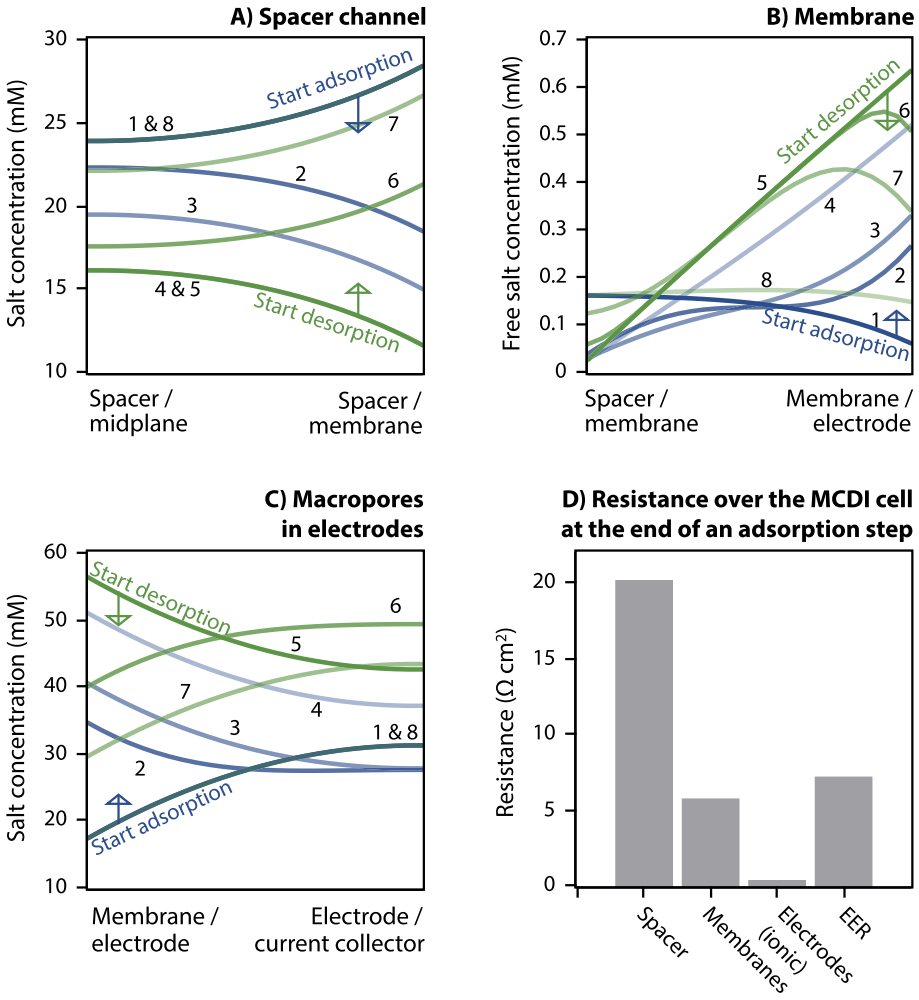

Fig. 6. Theoretical prediction of the salt concentration across, and the resistance in, the MCDI cell from the start of the adsorption step (1) until the end of a desorption step (8) ($c_{inflow} = 20$ mM, $I = 19$ A/m^2). For the times associated with each curve in panels a–c see main text.

the transport model with experimental data of CCCD experiments (Section 4), now we can use the theory to predict the resistances across the MCDI cell during desalination of brackish water. Therefore, we will simulate the limit cycle of an MCDI experiment, with the same operational scheme as shown in Fig. 4, the parameters as listed in Table 1, a flow of 7.5 mL/min/cell, and an inflow salt concentration of $c_{inflow} = 20$ mM.

Fig. 6 shows the salt concentration profiles across the spacer channel and the electrodes, as well as the free salt concentration across the membranes (which is the counterion concentration minus the fixed membrane charge density, equal to the co-ion concentration), at different moments during the adsorption and desorption step. During the adsorption step, the salt concentration in the electrode (macropores) increases, while the salt concentration in the spacer channel goes down at the same time. The reverse is observed during the desorption step. Profiles shown in Fig. 6 a–c are given to illustrate the development of concentrations in the different domains and are related to the following moments during the adsorption cycle: a) 0, 4, 8, 98 s after start of adsorption, and 0, 4, 12 and 298 s after start of desorption. For b) 0, 10, 18, 98 s; 0, 2, 8, 260 s; c) 0, 8, 18, 98 s; 0, 10, 240, 298 s.

Fig. 6D shows the ionic resistances in the spacer channel, the membranes, and in the electrodes, as well as the *EER*, all at the start of a desorption step. Clearly, the ionic resistance across the spacer is the highest of all resistances, while the ionic resistance in the electrodes is negligible. The calculated resistance across the membranes (5.6 Ω cm^2) is similar to values reported by Tuan et al. (2006) and Długołęcki et al. (2010). Note that the calculations show that the electronic and ionic resistances do not significantly change during the cycle. However, values for the resistances shown in Fig. 6D can be completely different in other situations, for instance when the salt concentration in the macropores of the electrodes decreases to values close to zero, such as in CDI without membranes.

6. Improved system design: increased electrode thickness

After identifying that the resistances are mainly located in the spacer channel, the membranes and the external electrical circuit, and not in the electrodes, we can use this information to improve the (M)CDI cell design or operation. Options include the study of the *EER*, with the aim to reduce it, or the spacer channel resistance (e.g., by using ion-conducting spacers (Liang et al., 2013), spacers packed with granular activated carbon (Bian et al., 2015) or profiled membranes (Vermaas et al., 2011)). Here, as an example, we will focus instead on the electrode. Fig. 6D suggests that it should be possible to increase the electrode thickness and consequently the cell capacity (thus requiring less switches between adsorption and desorption), while keeping the energy consumption per mol salt removed the same. To test this hypothesis, we performed

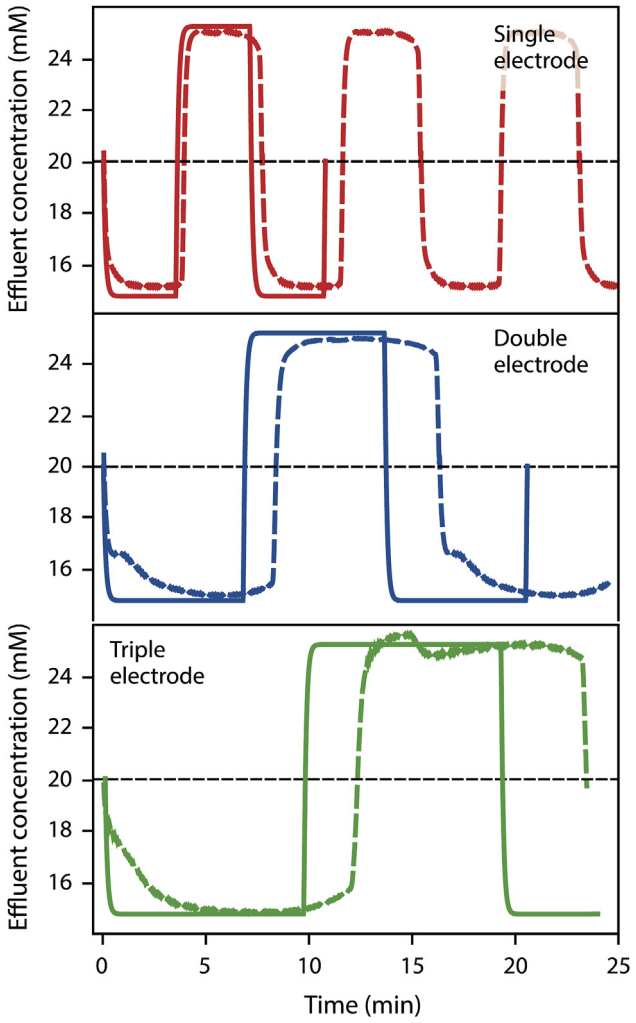

Fig. 7. Effluent salt concentration as function of time for MCDI with single, double and triple electrode thickness (c_{inflow} = 20 mM, I = 19 A/m^2). Dashed lines: experimental data. Solid lines: theory.

experiments in MCDI where we doubled and tripled the electrode thickness, by placing two respectively three electrodes, with the thickness as listed in Table 1, on top of one another, and we measure the energy requirements.

To this end, we conducted F-CCCD experiments with the same operational scheme and electrodes as those described for the F-CCCD experiments in section 4 (I = 19 A/m^2). The results for the effluent concentration as function of time are shown in Fig. 7. As Fig. 7 shows, increasing the electrode thickness indeed results in longer cycles. Comparing the data with the theory, the model closely predicts the desalination degree, but underpredicts the cycle time quite significantly.

For the experiments shown in Fig. 7, we calculated the energy consumption by integrating the electrical power (current multiplied by cell voltage) over time, and dividing the resulting value by the salt adsorption in a cycle (in mol). The resulting values are

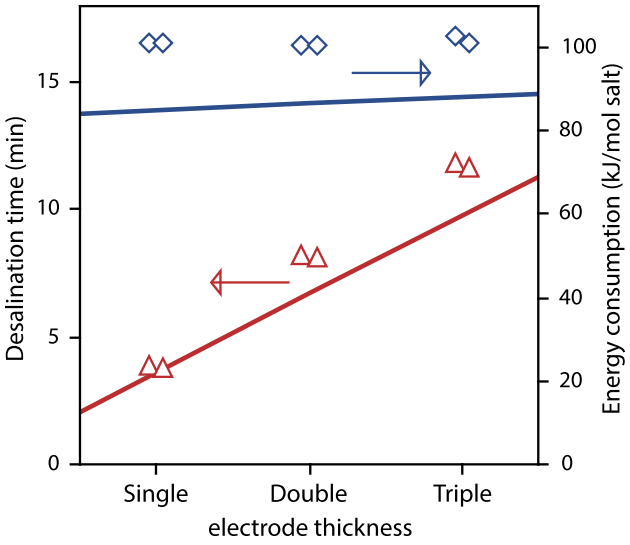

Fig. 8. Desalination time and energy consumption for single, double and triple electrode thickness (c_{inflow} = 20 mM, I = 19 A/m^2). Solid lines: theory.

plotted in Fig. 8[2]. Note that in this work, we report the energy consumption in dimension kJ/mol salt, while in previous work the dimension kT/ion was used. One can recalculate values in kT/ion to values in kJ/mol salt by multiplication with a factor $2 \cdot R \cdot T/1000 \sim 5$.

Interestingly, the energy consumption of MCDI due to resistances over the different elements of the cell, as presented in Fig. 6D, is only 6.1 kJ/mol salt. The additional energy requirements are due to the Donnan potentials at the membrane interfaces, and the Donnan and Stern potentials in the electrodes. These energies all relate to the thermodynamics of ion removal and storage, not to transport resistances. Both data and theory presented in Fig. 8 indicate that increasing the electrode thickness results in longer periods of desalination, i.e., we have the same desalination rate for a longer period of time with only a very slight increase of the energy consumption.

7. Conclusion

In the present work, we outlined a methodology to identify the ionic and electronic resistances in Membrane Capacitive Deionization (MCDI). To calculate the ionic resistances, we set up a transport model for the MCDI cell, with a fully discretized spacer channel, membrane and porous carbon electrode, coupled to the improved modified Donnan model. We show that the resulting model can be fitted to experimental data, and that we can use this theory to calculate the ionic resistances across the different elements in the MCDI cell. Furthermore, we presented a novel approach to measure the external electronic resistances, as well as the spacer properties in the MCDI cell.

For the MCDI cell studied, the resistances are mainly located in the spacer channel and in the external electrical circuit, while the resistance in the macropores of the electrodes is significantly lower. This finding predicts, and is also validated by our experimental work, that one can double or triple the electrode thickness without significantly increasing the electrical energy input per mol salt removed. Therefore, one can operate the cell with longer periods of desalination, switching less frequently between adsorption and desorption steps, without an extra energy penalty. Furthermore, our results show that, if we want to reduce the resistances in the MCDI cell, we have to focus, in order of priority, on the spacer channel, the external electrical circuit and then on the membranes.

[2] Note that experiments with double and triple electrode thickness were performed with 2 respectively 1 cell(s) assembled in a stack, instead of the 4 cells in the single electrode experiments. This leads to a different value for the *EER*. To evaluate energy consumption in Fig. 8, we corrected the data to 4 cells using results of a technical study that *EER* depends on N_s according to $EER = \alpha/N_s + \beta$ with α = 17.1 Ω cm^2 and β = 2.7Ω cm^2.

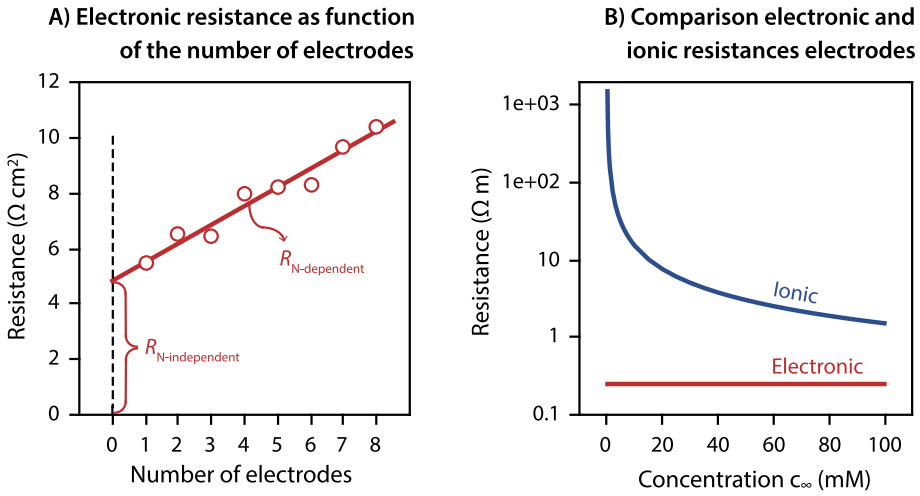

Fig. 9. A) Electronic resistance over different numbers of electrodes, and B) Comparison between the electronic and ionic resistance in the electrodes as function of the salt concentration c_∞.

Acknowledgment

This work was performed in the cooperation framework of Wetsus, European Centre of Excellence for Sustainable Water Technology (www.wetsus.nl). Wetsus is co-funded by the Dutch Ministry of Economic Affairs and Ministry of Infrastructure and Environment, the Province of Fryslân, and the Northern Netherlands Provinces. The authors like to thank the participants of the research theme Capacitive Deionization for the fruitful discussions and their financial support. We thank R.M. Wagterveld (Wetsus) for his ideas to measure the electronic resistances over the (M)CDI stack.

Appendices

A. Improved modified Donnan model

To describe the salt adsorption and charge density in the electrical double layers (EDLs), formed in the micropores of the porous carbon electrodes, we use the improved modified Donnan (i-mD) model (Biesheuvel et al., 2014).

Applied to a 1:1 salt with a charge neutral macropore electrolyte, the i-mD model relates the ion concentration in the micropores, $c_{mi,i}$, to the salt concentration in the macropores, c_{mA}, according to

$$c_{mi,i} = c_{mA} \cdot \exp(-z_i \cdot \Delta\phi_D + \mu_{att}), \tag{29}$$

where z_i is the charge of the ion and $\Delta\phi_D$ the Donnan potential. The Donnan potential, $\Delta\phi_D$, is dimensionless and can be multiplied with the thermal voltage, V_T, to obtain a voltage with dimension V. The attraction term μ_{att} is a function of the micropore ion correlation energy, E, and the total ion concentration in the micropores, $c_{ions,mi}$, and is given by

$$\mu_{att} = \frac{E}{c_{ions,mi}}. \tag{30}$$

In the micropores, the ionic charge density, σ_{mi}, can be calculated by Eq. (4). For a 1:1 salt, the concentration of ions in the micropores, $c_{ions,mi}$, can be computed as function of the charge density in the micropores, σ_{mi}, according to

$$c_{ions,mi}^2 = \sigma_{mi}^2 + (2 \cdot c_{mA} \cdot \exp(\mu_{att}))^2. \tag{31}$$

The Stern potential, $\Delta\phi_{St}$, is a function of the ionic charge in the micropores and is given by

$$\sigma_{mi} \cdot F = -C_{St,vol} \cdot \Delta\phi_{St} \cdot V_T, \tag{32}$$

with $C_{St,vol}$ the volumetric Stern capacity in F/m^3, given by the empirical relation

$$C_{St,vol} = C_{St,vol,0} + \alpha \cdot \sigma_{mi}^2, \tag{33}$$

where α is a parameter to relate the Stern capacitance to the micropore charge density and $C_{St,vol,0}$ the Stern capacitance in the zero-charge limit.

At equilibrium, there is no net transport of ions from the spacer channel into the micropores, and the salt concentration in the macropores, c_{mA}, is equal to the concentration outside the electrode, c_∞. Since the electrolyte only contains a monovalent salt (KCl), there the concentration of K^+ equals the concentration of Cl^-, both equal to the salt concentration, c_∞. Eqs. (4) and (29) can be combined to describe $c_{ions,mi}$ and σ_{mi} as function of $\Delta\phi_D$ and μ_{att} according to

$$\sigma_{mi} = c_{cation,mi} - c_{anion,mi} = -2 \cdot c_\infty \cdot \exp(\mu_{att}) \cdot \sinh(\Delta\phi_D), \tag{34}$$

$$c_{ions,mi} = c_{cation,mi} + c_{anion,mi} = 2 \cdot c_\infty \cdot \exp(\mu_{att}) \cdot \cosh(\Delta\phi_D). \tag{35}$$

From now on, we assume that both oppositely polarized electrodes in a CDI cell are equal, e.g. they have the same geometric and material characteristics. In addition to the assumption of a 1:1 salt, this assumption allows us to model the CDI cell at equilibrium as a symmetric cell, and we only have to calculate the salt adsorption and charge density in one electrode. With this assumption, the cell voltage relates to the Donnan and Stern potentials by

$$V_{cell} = 2 \cdot V_T \cdot |\Delta\phi_D + \Delta\phi_{St}|. \tag{36}$$

To calculate the theoretical charge efficiency of the system, that is, the number of salt molecules adsorbed over the number of electrons transported from one electrode to the other, we use the relation

$$\Lambda = \frac{c^{ads}_{ions,mi} - c^{des}_{ions,mi}}{\left|\sigma^{ads}_{mi} - \sigma^{des}_{mi}\right|}, \tag{37}$$

where $c^{ads}_{ions,mi}$ ($c^{des}_{ions,mi}$) is the concentration of ions in the micropores at the end of an adsorption (desorption) step. The concentration $c_{ions,mi}$ at the end of the desorption step equals $c_{ions,mi}$ at the beginning of an adsorption step. The charge density, Σ_F (in C/g), and the salt adsorption, Γ_{salt} (in mg/g), can be calculated according to

$$\Sigma_F = \frac{1}{2}\cdot F \cdot \nu_{mi} \cdot \left|\sigma^{ch}_{mi} - \sigma^{disch}_{mi}\right|, \tag{38}$$

$$\Gamma_{salt} = \frac{1}{2}\cdot \nu_{mi} \cdot \left(c^{ch}_{ions,mi} - c^{disch}_{ions,mi}\right). \tag{39}$$

Theoretical values for Σ_F, Γ_{salt} and Λ can be compared with experimental results to find appropriate values for the parameters E, $C_{St,vol,0}$, α and ν_{mi}, see Fig. 2 and Table 1.

B. Electronic resistance in porous electrodes

One of the underlying assumptions of the transport model is that, within the porous carbon electrodes, the electronic resistance (resistance for flow of electronic charge through carbon matrix) is zero. To verify whether this assumption is valid, we measured the electronic resistance over different numbers of electrodes, which are connected via current collectors and cables to an Agilent Milliohmmeter 4338B. This device measures the resistance by applying a sinusoidal potential excitation with a frequency of 1 kHz and measuring the current. In this experiment, a number of wet electrodes is placed on top of each other, without spacer layers, between two current collectors and is slightly compressed by exerting a pressure of 0.29 bar. The results of the measured resistance, multiplied by the electrode surface area of $A_{cell} = 33.8$ cm^2, are shown in Fig. 9A.

As Fig. 9A shows, the resistance has a term independent of the number, N, of electrodes, given by the intercept, and a term linearly dependent on N, given by the slope. The first resistance is in the communal cables and connectors. The second term, which is N-dependent, must relate to an electronic resistance in the electrodes themselves, or to an electrode–electrode contact resistance. Therefore, the slope of Fig. 9A is equal to the electronic resistance per electrode, $R_{N-dependent}$, which is 0.67 Ω cm^2/electrode. Dividing $R_{N-dependent}$ by the thickness of one electrode ($L = 254$ μm), results in an electronic resistance of 0.26 Ω m, as shown in Fig. 9B. We can compare this value with the ionic resistance in the electrodes, $R_{ionic,electrodes}$, as given by

$$R_{ionic,electrodes} = \frac{V_T}{2\cdot p_{mA}\cdot c_\infty \cdot D \cdot F} \tag{40}$$

where V_T, p_{mA}, D and F refer to parameters as used in Section 2 and listed in Table 1.

In Fig. 9B we compare the electronic and ionic resistance in the electrodes, as function of c_∞. We observe that, for $c_\infty = 20$ mM, which is the inflow concentration in the experiments presented in Section 5 and 6, the ionic resistance in the electrode is a factor 30 higher than the electronic resistance. This ratio drops with increasing c_∞ but even at 100 mM, the ratio is still a factor of 10. Consequently, we consider the assumption of zero electronic resistance in the porous carbon electrodes to be valid.

C. Electrode preparation

The experimental work was conducted with home-made porous carbon electrodes (Porada et al., 2013; Kim et al., 2015). The electrodes were fabricated by mixing activated carbon (YP−50F, Kuraray, Japan), carbon black (Vulcan XC72R, Cabot Corp., Boston, MA), and a binder (85:5:10 in weight ratio). This binder, polyvinylidene fluoride (PVDF, Kynar HSV 900, Arkema Inc., Philadelphia, PA), was dissolved in N-methyl-2-pyrrolidone (NMP) and the mixture was vigorously stirred. After mixing the activated carbon, the carbon black and the binder solution, the solution was ground in a ball-grinding machine for 40 min (500 rpm). The resulting slurry was cast on a glass plate, which was, after casting, directly transferred into a deionized water bath, to solidify the binder. The resulting carbon films were cut into electrodes of 6*6 cm^2 with a small square of 1.5*1.5 cm^2 located in the center. The electrodes were dried at 105 °C, cooled down in a desiccator and weighed.

D. Equilibrium CDI experiments

To find values for the parameters $C_{St,vol,0}$, α, E and ν_{mi}, as used in the i-mD model, we conducted equilibrium CDI experiments, so we excluded the membranes, according to the following experimental procedure. A stack of $N_s = 4$ CDI cells, each cell consisting of a pair of porous carbon electrodes (see Appendix C), a pair of graphite current collectors and a spacer (AP20, Glass Fiber Filter, Millipore, MA), was placed in a polymethylmethacrylate (PMMA) housing. A solution of potassium chloride, KCl, was pumped from a recirculation vessel of 10 L, into the housing, through the spacer channels of the CDI cells, leaving the cell passing a conductivity sensor and a pH sensor, back to the recirculation vessel. The outlet conductivity and pH were online monitored with a sampling time of 1 s. KCl solutions of 20 and 100 mM were prepared and were continuously purged with nitrogen, in order to avoid the presence of oxygen in the electrolyte. While the solution was flowing through the cell, the cell voltage was controlled with a potentiostat (IviumStat, Ivium Technologies, the Netherlands). Alternately, a charging voltage, V_{ch}, and a discharge voltage, V_{disch}, were set for 20 min each, in order to reach equilibrium, that means, the electrodes became fully saturated with salt (at the end of the charging step), or were fully discharged (at the end of a discharging step), and there is no longer transport of salt between spacer and electrode. Experiments were conducted with different, distinct, values of V_{ch}, of 0.2, 0.4, 0.6, 0.8, 1 and 1.2 V, while the discharge voltage was always set to 0 V. For every experiment with a different charging voltage, we run 4 cycles of charging and discharging, to attain the situation that the results of the last cycle become equal to the results of the previous cycle, i.e., we reached the limit cycle. Only the data of the final cycles were processed.

Of every experiment, the current, the effluent conductivity and the pH were recorded. The current was integrated over time, both for the charging and discharging step of each experiment, to obtain the charge with dimension C. To calculate the charge density, Σ_F, in C/g, the charge was divided by the total mass of the dry electrodes. The effluent conductivity is recalculated to salt concentration making use of a calibration curve. Thereafter, the difference between the inflow and effluent salt concentration was integrated over time, and multiplied by the water flow rate, resulting in the salt adsorption, or desorption, with dimension mol. Multiplying this salt adsorption with the molar mass of KCl and dividing by the total electrode mass, results in the salt adsorption, Γ_{salt} with dimension mg/g. Charge efficiency Λ can be calculated according to

$$\Lambda = \frac{\Gamma_{salt}}{\Sigma_F}\cdot F. \tag{41}$$

E. Calculating the micro-, meso-, and macroporosity

For the transport model, we require values for the micro-, meso- and macroporosity, as listed in Table 1. To calculate the microporosity, p_{mi}, we multiply the theoretically derived value for v_{mi} (see Appendix D) with the electrode mass density in g/mL, ρ_{elec}.

As explained by Kim et al. (2015), the value of v_{mi} calculated by fitting the i-mD model to the data, resulting in $v_{mi} = 0.40$ mL/g (defined per mass of electrode material), is lower than the pore volume determined by gas sorption analysis (and using the NLDFT model for evaluation) of the porous carbon electrode, which is $v_{GSA} = 0.48$ mL/g (again defined per mass of electrode material) (Note that this value is obtained from gas adsorption analysis of the entire electrode, not of a pristine powder). Because of the difference between v_{mi} and v_{GSA}, the term mesoporosity was introduced, referring to the pores which are not used for transport and where also no EDLs are formed, but which are filled up with electrolyte. So, the difference between v_{mi} and v_{GSA} is multiplied with ρ_{elec} to obtain the mesoporosity, p_{meso}.

The macroporosity, p_{mA}, follows from the relation $p_{mi} + p_{meso} + p_{sk} + p_{mA} = 1$, where p_{sk} is the volume fraction of "skeleton" in the electrode, which in turn can be calculated by dividing ρ_{elec} by ρ_{sk}, the mass density of the skeleton material. The density $\rho_{sk} = 1.93$ g/mL is obtained from $\rho_{sk} = m_c \cdot \rho_c + (1 - m_c) \cdot \rho_b$ where m_c is the weight fraction of two carbon constituents together (activated carbon and carbon black), $m_c = 0.9$, ρ_c the mass density of the carbon, $\rho_c = 1.95$ g/mL, and ρ_b the density of the binder, $\rho_b = 1.78$ g/mL (Porada et al., 2013).

References

Andersen, M.B., van Soestbergen, M., Mani, A., Bruus, H., Biesheuvel, P.M., Bazant, M.Z., 2012. Current-induced membrane discharge. Phys. Rev. Lett. 109, 108301.

Avraham, E., Bouhadana, Y., Soffer, A., Aurbach, D., 2009. Limitation of charge efficiency in capacitive deionization. J. Electrochem. Soc. 156, 95–99.

Bian, Y., Yang, X., Liang, P., Jiang, Y., Zhang, C., Huang, X., 2015. Enhanced desalination performance of membrane capacitive deionization cells by packing the flow chamber with granular activated carbon. Water Res. 85, 371–376.

Biesheuvel, P.M., Porada, S., Levi, M., Bazant, M.Z., 2014. Attractive forces in microporous carbon electrodes for capacitive deionization. J. Solid State Electrochem. 18, 1365–1376.

Bouhadana, Y., Ben-Tzion, M., Soffer, A., Aurbach, D., 2011. A control system for operating and investigating reactors: the demonstration of parasitic reactions in the water desalination by capacitive de-ionization. Desalination 268, 253–261.

Choi, J.-H., 2014. Comparison of constant voltage (CV) and constant current (CC) operation in the membrane capacitive deionisation process. Desalination Water Treat. http://dx.doi.org/10.1080/19443994.2014.942379.

de Levie, R., 1963. On porous electrodes in electrolyte solutions — I,II,III. Electrochim. Acta 8, 751–780.

Demirer, O.N., Naylor, R.M., Rios Perez, C.A., Wilkes, E., Hidrovo, C., 2013. Energetic performance optimization of a capacitive deionization system operating with transient cycles and brackish water. Desalination 314, 130–138.

Długołęcki, P., Ogonowski, P., Metz, S.J., Saakes, M., Nijmeijer, K., Wessling, M., 2010. On the resistances of membrane, diffusion boundary layer and double layer in ion exchange membrane transport. J. Membr. Sci. 349, 369–379.

Długołęcki, P., van der Wal, A., 2013. Energy recovery in membrane capacitive deionization. Environ. Sci. Technol. 47, 4904–4910.

Dykstra, J.E., Biesheuvel, P.M., Bruning, H., Ter Heijne, A., 2014. Theory of ion transport with fast acid-base equilibrations in bioelectrochemical systems. Phys. Rev. E 90, 013302.

Galama, A.H., Post, J.W., Cohen Stuart, M.A., Biesheuvel, P.M., 2013. Validity of the Boltzmann equation to describe Donnan equilibrium at the membrane–solution interface. J. Membr. Sci. 442, 131–139.

Giera, B., Henson, N.J., Kober, E.M., Shell, M.S., Squires, T.M., 2015. Electric double layer structure in primitive model electrolytes: comparing molecular dynamics with local-density approximations. Langmuir 31, 3553–3562, 150227102447002.

Huang, Z.H., Wang, M., Wang, L., Kang, F.Y., 2012. Relation between the charge efficiency of activated carbon fiber and its desalination performance. Langmuir 28, 5079–5084.

Jeon, S.I., Park, H.R., Yeo, J.G., Yang, S., Cho, C.H., Han, M.H., Kim, D.K., 2013. Desalination via a new membrane capacitive deionization process utilizing flow-electrodes. Energy & Environ. Sci. 6, 1471–1475.

Johnson, A.M., Newman, J., 1971. Desalting by means of porous carbon electrodes. J. Electrochem. Soc. 118, 510–517.

Jung, H.H., Hwang, S.W., Hyun, S.H., Lee, K.H., Kim, G.T., 2007. Capacitive deionization characteristics of nanostructured carbon aerogel electrodes synthesized via ambient drying. Desalination 216, 377–385.

Kim, T., Dykstra, J.E., Porada, S., van der Wal, A., Yoon, J., Biesheuvel, P.M., 2015. Enhanced charge efficiency and reduced energy use in capacitive deionization by increasing the discharge voltage. J. Colloid Interface Sci. 446, 317–326.

Kim, T., Yoon, J., 2013. Relationship between capacitance of activated carbon composite electrodes measured at a low electrolyte concentration and their desalination performance in capacitive deionization. J. Electroanal. Chem. 704, 169–174.

Kim, Y.J., Choi, J.H., 2010. Improvement of desalination efficiency in capacitive deionization using a carbon electrode coated with an ion-exchange polymer. Water Res. 44, 990–996.

Lee, J.-B.B., Park, K.-K.K., Eum, H.-M.M., Lee, C.-W.W., 2006. Desalination of a thermal power plant wastewater by membrane capacitive deionization. Desalination 196, 125–134.

Lee, J.-H.H., Bae, W.-S.S., Choi, J.-H.H., 2010. Electrode reactions and adsorption/desorption performance related to the applied potential in a capacitive deionization process. Desalination 258, 159–163.

Lei, H., Yan, T., Wang, H., Shi, L., Zhang, J., Zhang, D., 2015. Graphene-like carbon nanosheets prepared by a Fe-catalyzed glucose-blowing method for capacitive deionization. J. Mater. Chem. A 3, 5934–5941.

Li, H., Pan, L., Zhang, Y., Zou, L., Sun, C., Zhan, Y., Sun, Z., 2010. Kinetics and thermodynamics study for electrosorption of NaCl onto carbon nanotubes and carbon nanofibers electrodes. Chem. Phys. Lett. 485, 161–166.

Liang, P., Yuan, L., Yang, X., Zhou, S., Huang, X., 2013. Coupling ion-exchangers with inexpensive activated carbon fiber electrodes to enhance the performance of capacitive deionization cells for domestic wastewater desalination. Water Res. 47, 2523–2530.

Mirzadeh, M., Gibou, F., Squires, T.M., 2014. Enhanced charging kinetics of porous electrodes: surface conduction as a short-circuit mechanism. Phys. Rev. Lett. 113, 097701.

Mossad, M., Zou, L., 2013. Evaluation of the salt removal efficiency of capacitive deionisation: kinetics, isotherms and thermodynamics. Chem. Eng. J. 223, 704–713.

Omosebi, A., Gao, X., Landon, J., Liu, K., 2014. Asymmetric electrode configuration for enhanced membrane capacitive deionization. ACS Appl. Mater. Interfaces 6, 12640–12649.

Paz-Garcia, J.M., Dykstra, J.E., Biesheuvel, P.M., Hamelers, H.V.M., 2015. Energy from CO2 using capacitive electrodes – a model for energy extraction cycles. J. Colloid Interface Sci. 442, 103–109.

Pell, W.G., Conway, B.E., Marincic, N., 2000. Analysis of non-uniform charge/discharge and rate effects in porous carbon capacitors containing sub-optimal electrolyte concentrations. J. Electroanal. Chem. 491, 9–21.

Porada, S., Borchardt, L., Oschatz, M., Bryjak, M., Atchison, J.S., Keesman, K.J., Kaskel, S., Biesheuvel, P.M., Presser, V., 2013. Direct prediction of the desalination performance of porous carbon electrodes for capacitive deionization. Energy & Environ. Sci. 6, 3700–3712.

Porada, S., Sales, B.B., Hamelers, H.V.M., Biesheuvel, P.M., 2012. Water desalination with wires. J. Phys. Chem. Lett. 3, 1613–1618.

Posey, F.A., Morozumi, T., 1966. Theory of potentiostatic and galvanostatic charging of the double layer in porous electrodes. J. Electrochem. Soc. 113, 176–184.

Prehal, C., Weingarth, D., Perre, E., Lechner, R.T., Amenitsch, H., Paris, O., Presser, V., 2015. Tracking the structural arrangement of ions in carbon supercapacitor nanopores using in-situ small-angle X-ray scattering. Energy Environ. Sci. http://dx.doi.org/10.1039/C5EE00488H.

Qu, Y., Baumann, T.F., Santiago, J.G., Stadermann, M., 2015. Characterization of resistances of a capacitive deionization system. Environ. Sci. Technol. 49, 9699–9706, 150727105548004.

Rica, R.A., Ziano, R., Salerno, D., Mantegazza, F., Brogioli, D., 2012. Thermodynamic relation between voltage-concentration dependence and salt adsorption in electrochemical cells. Phys. Rev. Lett. 109, 156103.

Suss, M.E., Baumann, T.F., Bourcier, W.L., Spadaccini, C.M., Rose, K.A., Santiago, J.G., Stadermann, M., 2012. Capacitive desalination with flow-through electrodes. Energy & Environ. Sci. 5, 9511–9519.

Suss, M., Porada, S., Sun, X., Biesheuvel, M., Yoon, J., Presser, V., 2015. Water desalination via capacitive deionization: what is it and what can we expect from it? Energy Environ. Sci. http://dx.doi.org/10.1039/C5EE00519A.

Tang, W., Kovalsky, P., He, D., Waite, T.D., 2015. Fluoride and nitrate removal from brackish groundwaters by batch-mode capacitive deionization. Water Res. 84, 342–349.

Tsouris, C., Mayes, R., Kiggans, J., Sharma, K., Yiacoumi, S., DePaoli, D., Dai, S., 2011. Mesoporous carbon for capacitive deionization of saline water. Environ. Sci. Technol. 45, 10243–10249.

Tuan, L.X., Verbanck, M., Buess-Herman, C., Hurwitz, H., 2006. Properties of CMV cation exchange membranes in sulfuric acid media. J. Membr. Sci. 284, 67–78.

van Limpt, B., van der Wal, A., 2014. Water and chemical savings in cooling towers by using membrane capacitive deionization. Desalination 342, 148–155.

Vermaas, D.A., Saakes, M., Nijmeijer, K., 2011. Power generation using profiled membranes in reverse electrodialysis. J. Membr. Sci. 385–386, 234–242.

Zhao, R., Biesheuvel, P.M., van der Wal, A., 2012. Energy consumption and constant current operation in membrane capacitive deionization. Energy & Environ. Sci. 5, 9520–9527.

Zhao, R., Porada, S., Biesheuvel, P.M., van der Wal, A., 2013a. Energy consumption in membrane capacitive deionization for different water recoveries and flowrates, and comparison with reverse osmosis. Desalination 330, 35–41.
Zhao, R., Satpradit, O., Rijnaarts, H.H.M., Biesheuvel, P.M., van der Wal, A., 2013b. Optimization of salt adsorption rate in membrane capacitive deionization. Water Res. 47, 1941–1952.
Zhao, Y., Hu, X.M., Jiang, B.H., Li, L., 2014. Optimization of the operational parameters for desalination with response surface methodology during a capacitive deionization process. Desalination 336, 64–71.